



1 **The role of OCO-3 XCO₂ retrievals in estimating global ter-**
2 **restrial net ecosystem exchanges**

3 Xingyu Wang¹, Fei Jiang^{1,2,5,*}, Hengmao Wang¹, Zhengqi Zhang¹, Mousong Wu¹, Jun Wang¹, Wei
4 He⁴, Weimin Ju^{1,5}, Jing M. Chen^{3,6}

5 ¹Jiangsu Provincial Key Laboratory of Geographic Information Science and Technology, Interna-
6 tional Institute for Earth System Science, Nanjing University, Nanjing, 210023, China.

7 ²Jiangsu Center for Collaborative Innovation in Geographical Information Resource Development
8 and Application, Nanjing, 210023, China.

9 ³Department of Geography and Planning, University of Toronto, Toronto, Ontario M5S3G3, Canada.

10 ⁴Zhejiang Carbon Neutral Innovation Institute, Zhejiang University of Technology, Hangzhou,
11 Zhejiang 310014, China.

12 ⁵Frontiers Science Center for Critical Earth Material Cycling, Nanjing University, Nanjing, 210023,
13 China.

14 ⁶School of Geographical Sciences, Fujian Normal University, Fuzhou, 350007, China

15
16 *Corresponding author: Fei Jiang (jiangf@nju.edu.cn)



25 **Abstract**

26 Satellite-based column-averaged dry air CO₂ mole fraction (XCO₂) retrievals are frequently used to
27 improve the estimates of terrestrial net carbon exchanges (NEE). The Orbiting Carbon Observatory 3
28 (OCO-3) satellite, launched in May 2019, was designed to address important questions about the dis-
29 tribution of carbon fluxes on Earth, but its role in estimating global terrestrial NEE remains unclear.
30 Here, using the Global Carbon Assimilation System, version 2, we investigate the impact of OCO-3
31 XCO₂ on the estimation of global NEE by assimilating the OCO-3 XCO₂ retrievals alone and in com-
32 bination with the OCO-2 XCO₂ retrievals. The results show that when only the OCO-3 XCO₂ is as-
33 similated (Exp_OCO3), the estimated global land sink is significantly lower than that from the OCO-
34 2 experiment (Exp_OCO2). The estimate from the joint assimilation of OCO-3 and OCO-2
35 (Exp_OCO3&2) is comparable on a global scale to that of Exp_OCO2. However, there are significant
36 regional differences. Compared to the observed global annual CO₂ growth rate, Exp_OCO3 has the
37 largest bias, and Exp_OCO3&2 shows the best performance. Furthermore, validation with independent
38 CO₂ observations shows that the biases of the Exp_OCO3 are significantly larger than those of
39 Exp_OCO2 and Exp_OCO3&2 at mid and high latitudes, probably due to the fact that OCO-3 only
40 has observations from 52°S to 52°N. Our study indicates that assimilating OCO-3 XCO₂ retrievals
41 alone leads to an underestimation of land sinks at high latitudes, and that a joint assimilation of OCO-
42 2 and OCO-3 XCO₂ retrievals is required for a better estimation of global terrestrial NEE.

43

44

45

46

47

48

49

50

51



52 **1 Introduction**

53 The rising of the carbon dioxide (CO₂) concentration in the Earth's atmosphere in recent decades,
54 which is mainly caused by human activities, such as the burning of fossil fuels, deforestation and land-
55 use change, has become a global concern (Hansen et al., 2013). Terrestrial ecosystems and oceans
56 together absorb about 56 per cent of anthropogenic CO₂ emissions (Friedlingstein et al., 2023). Among
57 them, terrestrial ecosystems play a crucial role in regulating the atmospheric CO₂ concentration. How-
58 ever, the carbon uptake capacity of terrestrial ecosystems varies considerably globally and regionally
59 (Bousquet et al., 2000; Takahashi et al., 2009; Piao et al., 2020). Therefore, accurate quantification of
60 global and regional terrestrial net ecosystem exchange (NEE) is very important to understand their role
61 and potential in regulating changes in the atmospheric CO₂ concentration.

62 Atmospheric inversion is a major method for estimating surface carbon fluxes from observations
63 of atmospheric CO₂ concentration (Enting and Newsam, 1990; Gurney et al., 2002; Thompson et al.,
64 2016; Jiang et al., 2021), but it is more effective at the global scale than at the regional scale. A large
65 number of previous studies have shown that different atmospheric inversion models can produce rela-
66 tively consistent global estimates of carbon fluxes, but their performance at regional scales is variable.
67 In regions such as the tropics, southern hemisphere oceans, and most continental interiors (South
68 America, Africa and boreal Asia), the reliability of atmospheric inversions varies considerably due to
69 the heterogeneous distribution of *in-situ* observations, leading to an increase in the uncertainty of car-
70 bon flux estimates (Peylin et al., 2013; Wang et al., 2019). The use of satellite observations to constrain
71 atmospheric inversions can be effective in improving carbon flux estimates because of their better
72 spatial coverage (Basu et al., 2013; Byrne et al., 2020; Jiang et al., 2021; Wang et al., 2022; He et al.,
73 2023a). The National Aeronautics and Space Administration (NASA) launched the Orbiting Carbon
74 Observatory 2 (OCO-2) satellite in 2014 (Crisp et al., 2017; Eldering et al., 2012, 2017), followed by
75 the Orbiting Carbon Observatory 3 (OCO-3) satellite in 2019 (Taylor et al., 2023). The OCO-2 satel-
76 lites have a high sensitivity to column-averaged dry air CO₂ mole fraction (XCO₂), a fine footprint,
77 and a good spatial coverage, and can therefore be used to better constrain surface carbon flux estimates.
78 In previous studies, many atmospheric inversion models have used the XCO₂ from the OCO-2 satel-
79 lites to estimate global (e.g., Crowell et al., 2019; Peiro et al., 2022; Byrne et al., 2023) and regional



80 (e.g., Palmer et al., 2019; Byrne et al., 2021; Philip et al., 2022; He et al., 2022; He et al., 2023a)
81 surface carbon fluxes. For example, Miller et al. (2018) evaluated the effectiveness of OCO-2 obser-
82 vations in constraining regional biospheric CO₂ fluxes. Their findings indicate that OCO-2 observa-
83 tions are most effective at continental and hemispheric scales. Byrne et al. (2022) utilised OCO-2 data
84 to fill a gap in station observations at high latitudes. Their study confirmed the presence of significant
85 and widely distributed early cold-season CO₂ emissions in the northeastern region of Eurasia. Further-
86 more, several studies have utilised OCO-2 XCO₂ data to investigate the impact of climate extremes on
87 terrestrial NEE, such as El Niño (e.g., Liu et al., 2017) and droughts (He et al., 2023 b; Chen et al.,
88 2024). OCO-3 introduces new technologies and observational methods to monitor CO₂ on Earth, of-
89 fering the same temporal and spatial resolution as OCO-2. It is aimed at detecting mid-latitude regions
90 where human CO₂ emissions are concentrated. However, few studies have used the OCO-3 XCO₂
91 retrievals to constrain global and regional surface carbon fluxes till now. Therefore, it is important to
92 investigate the impact of assimilating OCO-3 observations on the estimates of global and terrestrial
93 carbon sinks.

94 In this study, we used both OCO-2 and OCO-3 XCO₂ retrievals to invert global and regional
95 carbon fluxes for the period of 2020-2022 with the Global Carbon Assimilation System, version 2
96 (GCASv2) (Jiang et al., 2021). The XCO₂ retrievals from OCO-2 and OCO-3 were assimilated sepa-
97 rately and together in order to disentangle the effect of OCO-3 XCO₂ retrievals on the estimates of
98 global and regional terrestrial carbon sinks.

99

100 **2 Methods and data**

101 **2.1 Inversion method**

102 The Global Carbon Assimilation System, version 2 (GCASv2) (Jiang et al., 2021; Wang et al.,
103 2021) designed primarily for assimilating satellite XCO₂ retrievals was adopted in this study to invert
104 surface carbon fluxes. The system uses the Model for Ozone and Related Chemical Tracers, version 4
105 (MOZART-4; Emmons et al., 2010) to simulate three-dimensional atmospheric CO₂ concentrations,
106 and an ensemble square root filter (EnSRF; Whitaker and Hamill, 2002) to implement the inversion of
107 surface fluxes. GCASv2 is an upgrade from the GCAS (Zhang et al., 2015) that was established in



108 2015. GCASv2 is cyclic, with a two-step optimization strategy in each assimilation window (1 week),
109 where the first step is to optimize the carbon fluxes by assimilating the observations, and the second
110 step is to input the optimized carbon fluxes into the MOZART-4 model to obtain the initial field of the
111 next assimilation window. In order to reduce the effects of horizontal observation error correlation and
112 representativeness error, based on the optimal estimation theory (Miyazaki et al., 2012), the system
113 also performs a “super-observation” scheme, which combines multiple observations located within a
114 same model grid into a single high-precision “super-observation”. A two-layers localization scale was
115 adopted in GCASv2, which is used to select which observations in a grid to use for flux analysis for
116 each grid. More details of the system can be found in Jiang et al (2021).

117 **2.2 OCO-2 and OCO-3 XCO₂ retrievals**

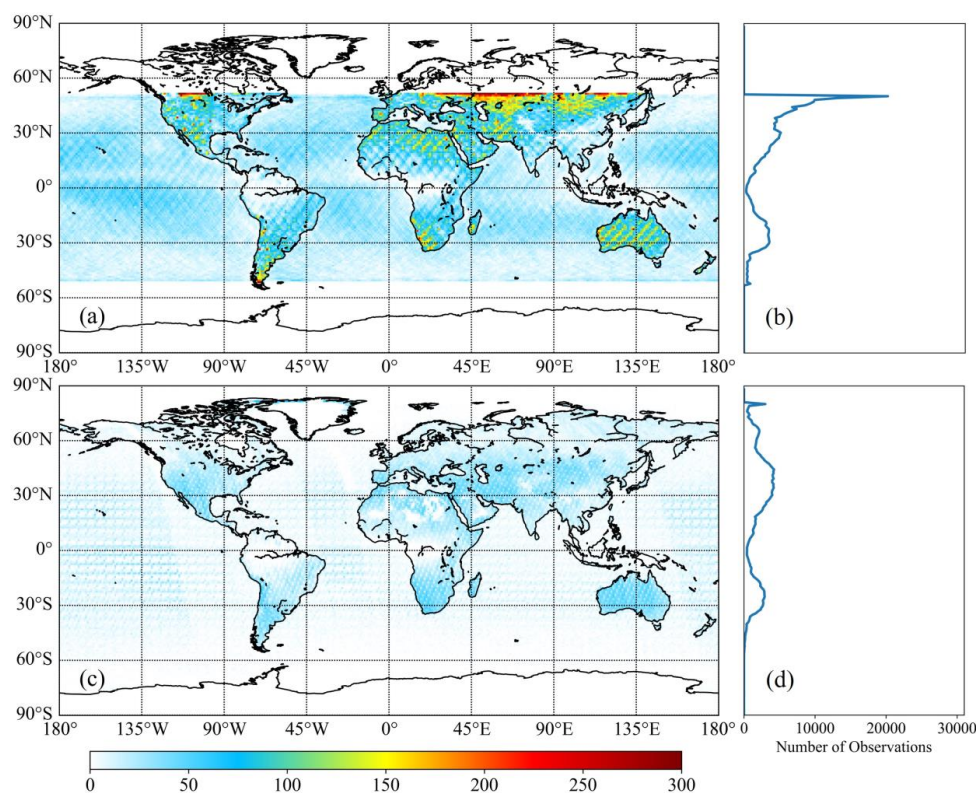
118 In July 2014, the Orbiting Carbon Observatory (OCO) -2 satellite was launched by NASA with
119 the primary objective of providing accurate space-based measurements to quantify changes in XCO₂.
120 The satellite is equipped with three high-resolution spectrometers that can detect two near-infrared
121 wavelength bands (1.61 μm and 2.06 μm) of sunlight reflectance spectra to observe CO₂. In May 2019,
122 NASA launched OCO-3 to the International Space Station (ISS) to detect CO₂ in mid-latitudes, where
123 human emissions are more concentrated. OCO-3 operates in a low-inclination orbit from 52°S to 52°N
124 and is equipped with three high-resolution spectrometers, providing the same temporal and spatial
125 resolutions as the OCO-2 satellites (Taylor et al., 2023). The detection target is also essentially the
126 same.

127 The XCO₂ data from OCO-3 and OCO-2 used in this study are bias-corrected products from
128 August 2019 to December 2022 at the image element level. The data are sourced from Version 10.4r
129 Level 2 Lite and Version 11.1r Level 2 Lite, respectively. Before using them in our inversion system,
130 it is essential to pre-process the data. First, both the land (Land Nadir + Land Glint, LNLG) and ocean
131 (Ocean Glint, OG) retrievals were adopted, and they were filtered using the parameter of XCO₂_qual-
132 ity_flag, which indicates the quality of the data. Only data with XCO₂_quality_flag=0 was selected for
133 assimilation in this study. Then, the LNLG and OG retrievals and their corresponding retrieval param-
134 eters were re-gridded to a spatial resolution of 1° × 1° and 5° × 5°, respectively. For the OG data, we
135 used a coarser re-gridding resolution, that is because the distribution of XCO₂ is more homogeneous



136 on sea than on land. Finally, both OCO-3 and OCO-2 XCO₂ retrievals were converted to the X2019
137 scale of the World Meteorological Organization (WMO) following Hall et al., (2021). Figure 1a and c
138 display the distribution and coverage of screened OCO-3 and OCO-2 XCO₂ retrievals from 2020 to
139 2022. Compared to OCO-2, OCO-3 has more observational data in the mid-latitudes of the northern
140 and southern hemispheres, especially in arid and semi-arid regions.

141 Following Jiang et al. (2022), the model-data mismatch errors were amplified by a factor on top
142 of the XCO₂ posterior errors, but with the minimum observation error setting to 1 ppm. It needs to be
143 noted that in the OCO-3 and OCO-2 products, the XCO₂ posterior errors of OG retrievals (0.48 ± 0.11
144 and 0.51 ± 0.15 ppm in 2020 for OCO-2 and OCO-3, respectively) are smaller than LNLG (0.54 ± 0.12
145 and 0.64 ± 0.18 ppm in 2020 for OCO-2 and OCO-3, respectively), but in fact, the observational error
146 should be greater at sea than on land (Peiro et al., 2022). Therefore, before multiplying by a uniform
147 factor, we increased the XCO₂ posterior errors of OG retrievals by 0.2 ppm. Taylor et al. (2023) re-
148 ported that the mean of the uncertainties for the OCO-2 and OCO-3 quality-filtered and bias-corrected
149 XCO₂ are 1.0 and 1.3 ppm, respectively. Considering that the global atmospheric transport model may
150 have an uncertainty of about 1.0 ppm (Lauvaux et al., 2009), thus in this study, we set the amplification
151 factor to be 3.5. Through this treatment, the mean model-data mismatch errors of LNLG and OG are
152 about 1.9 and 2.4 ppm for OCO-2, and 2.3 and 2.5 ppm for OCO-3, respectively.



153

154 **Figure1.** Data amount (the sum of 2020-2022) of XCO₂ in each grid cell (1° × 1°) and at each latitude used
155 in this study (a, b, OCO-3; c, d, OCO-2)

156 2.3 Prior carbon fluxes

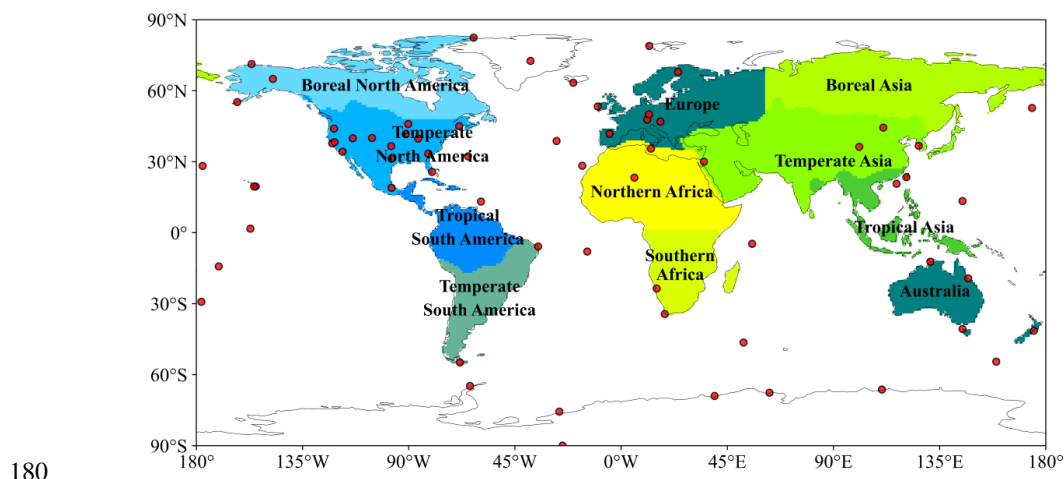
157 There are 4 prior carbon fluxes used in this study, which are terrestrial NEE, ocean-atmosphere
158 (OCN) carbon exchanges, fossil fuel and cement production (FOSSIL) carbon emissions, and biomass
159 combustion (FIRE) carbon emissions. The NEE were simulated using the BEPS model (Chen et al.,
160 2019). The OCN fluxes were derived from the mean of the JMA Ocean CO₂ Map (Iida et al., 2021),
161 which contains a global product with 1°×1° resolution (Globe, v2022) and another product for the
162 Northwest Pacific region with a resolution of 0.25°×0.25° (The western North Pacific, v2023). These
163 two products were integrated before they are used in this study. The FOSSIL carbon emissions were
164 obtained from GCP-GridFEDv2023.1 (Jones et al., 2021), which contains monthly global carbon emis-
165 sions from fossil fuels, cement production, and cement product weathering carbon sequestration at a



166 spatial resolution of $0.1^\circ \times 0.1^\circ$. The FIRE carbon emissions were obtained directly from the Global
167 Fire Emissions Database, Version 4.1 (GFED4.1s; Randerson et al., 2017).

168 2.4 Evaluation data and methods

169 Due to the significant spatial scale discrepancy between the inverted fluxes and the *in-situ* ob-
170 served fluxes, direct validation of the posterior Net Ecosystem Exchange (NEE) using observed data
171 is typically unattainable. However, we are able to indirectly evaluate the posterior fluxes by comparing
172 the atmospheric CO₂ concentrations, simulated with the posterior fluxes, against independent CO₂
173 measurements. (e.g., Jin et al., 2018; Wang et al., 2019; Feng et al., 2020; Jiang et al., 2021). In this
174 study, we used surface flask observations at 66 sites from the ObsPack dataset (ObsPack v9.1, Schuldt
175 et al., 2023) to independently assess the posterior fluxes. The screening of the 66 sites followed the
176 methodology of Jiang et al. (2022). The distribution of the 66 flask sites is shown in Figure 2. The
177 specific metrics assessed were the statistics of mean bias (BIAS), absolute bias (MAE), and root mean
178 square error (RMSE). We calculated annual BIAS, MAE, and RMSE globally, for different latitudinal
179 zones, and for different land areas.



180
181 **Figure2.** Distributions of the observation sites used for independent evaluation in this study and the 11 Trans-
182 Com-3 regions on land defined in Botta et al. (2012).

183



184 **3 Inversion experiments**

185 The GCASv2 system was run from 1 August 2019 to 31 December 2022. The initial five months
186 were designated as the spin-up stage, and the results from January 2020 to December 2022 were ana-
187 lyzed in this study. Three inversion experiments were conducted: (1) assimilation of OCO-3 XCO₂
188 retrievals alone (Exp_OCO3); (2) assimilation of OCO-2 XCO₂ retrievals alone (Exp_OCO2); and (3)
189 simultaneous assimilation of OCO-3 and OCO-2 XCO₂ retrievals (Exp_OCO3&2). In each experiment,
190 the methodology employed was consistent with that of previous studies (Peters et al., 2007; Jiang et
191 al., 2021, 2022), only the NEE and OCN fluxes were optimized, and the FIRE and FOSSIL emissions
192 are prescribed. Additionally, two forward simulations were conducted to obtain the prior and posterior
193 CO₂ concentrations, which were then compared with the independent CO₂ observations to assess the
194 posterior carbon fluxes. Following Jiang et al. (2022), MOZART-4 is driven by the 1.9° × 2.5° grids
195 version of the GEOS5 Global Atmosphere Forcing Data (Tilmes, 2016). It has a vertical level of 72
196 layers, and MOZART-4 uses the lowest 56 vertical levels of GEOS-5 and the same spatial resolution
197 with GEOS-5 data.

198

199 **4 Results and discussion**

200 **4.1 Global carbon budget**

201 Table 1 presents the prior and the posterior annual global carbon budgets from the 3 inversion
202 experiments during 2020-2022. The global terrestrial NEEs obtained from the Exp_OCO3,
203 Exp_OCO2, and Exp_OCO3&2 experiments are -3.41, -4.17, and -4.14 PgC yr⁻¹, respectively. The
204 global NEE inferred from the Exp_OCO3 is significantly weaker than those from Exp_OCO2 and
205 Exp_OCO3&2, and the latter two are comparable. For the OCN carbon sink, Exp_OCO3 has the
206 strongest sink but is closest to the a priori result, while Exp_OCO2 and Exp_OCO3&2 have essentially
207 the same sink. Combined with the FOSSIL and FIRE carbon emissions, the global net carbon fluxes
208 are 4.74, 5.55, 4.90, and 4.93 PgC yr⁻¹ for the a priori, Exp_OCO3, Exp_OCO2, and Exp_OCO3&2,
209 respectively. In comparison with the average atmospheric CO₂ growth rate of 4.96 PgC yr⁻¹ for 2020-
210 2022 given by the Global Carbon Budget 2023 (Friedlingstein et al., 2023), the results of
211 Exp_OCO3&2 are the closest, with a mean bias of 0.03 PgC yr⁻¹, whereas Exp_OCO3 has the largest



212 bias, with a deviation of 0.62 PgC yr^{-1} . This indicates that the carbon sinks in Exp_OCO3 may be
 213 significantly underestimated, and joint assimilation of OCO-2 and OCO-3 XCO₂ retrievals gives the
 214 best performance on a global scale.

215

216 **Table 1.** Global carbon budget estimated in the 3 inversion experiments (PgC yr^{-1}).

	Prior	Exp_OCO3	Exp_OCO2	Exp_OCO3&2
FOSSIL emissions			9.71	
FIRE emissions			1.97	
NEE	-4.10	-3.41	-4.17	-4.14
OCN fluxes	-2.84	-2.71	-2.61	-2.61
Global net carbon fluxes	4.74	5.55	4.90	4.93
Observed global CO ₂ growth rates			4.96	

217

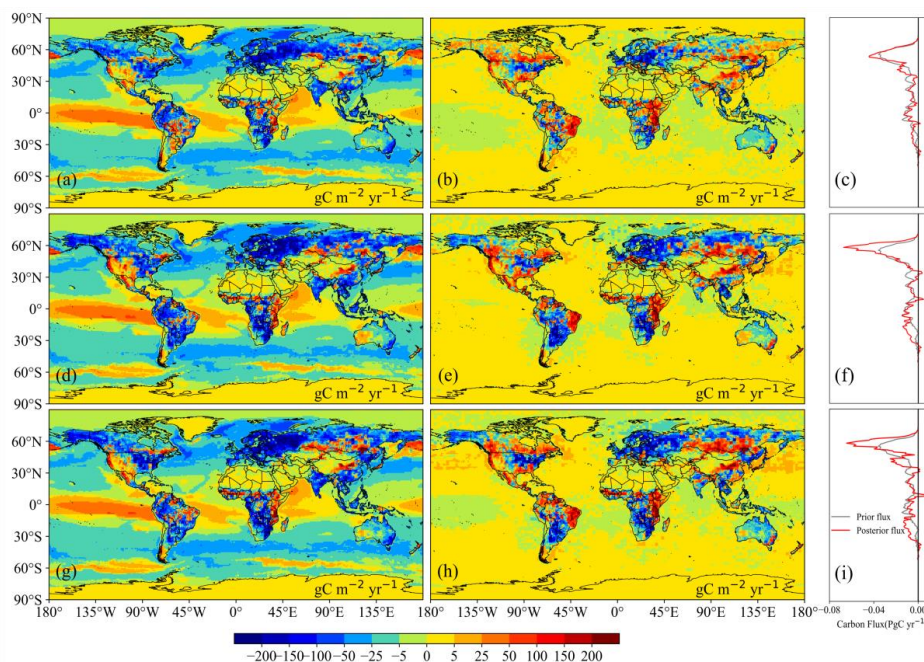
218 4.2 Regional NEE

219 Figure 3 shows the spatial distribution of annual mean posterior terrestrial fluxes and oceanic
 220 fluxes from the Exp_OCO3, Exp_OCO2, Exp_OCO3&2 and their differences against the a priori
 221 fluxes. Overall, the spatial distribution of carbon sources and sinks in terrestrial ecosystems obtained
 222 from different experiments is basically the same, with sinks in western North America (N. America),
 223 eastern Amazonia, parts of Siberia, parts of Northwest China, central and western Australia, and the
 224 Sahel region and eastern parts of Africa, while other areas are carbon sinks. However, the carbon
 225 sources/sinks obtained from Exp_OCO3 exhibit a markedly different strength compared to those de-
 226 rived from the other two experiments. Compared with the prior flux, the terrestrial carbon sinks in
 227 northeastern China, most of Europe, northern Siberia, the central and northeastern United States (US),
 228 and southern Africa increased significantly in all the 3 experiments. However, the increase in terrestrial
 229 carbon sinks in regions other than northeastern China in the Exp_OCO2 and Exp_OCO3&2 was
 230 greater than that in the Exp_OCO3. Meanwhile, in southern Canada, western and southern US, eastern
 231 Brazil and northern South America (S. America), the Sahel region and eastern parts of Africa, all the



232 3 inversion experiments show a significant decrease in the terrestrial carbon sink. The degree of change
 233 in the inversion results is more pronounced in the Exp_OCO2 and Exp_OCO3&2 than in the
 234 Exp_OCO3. Figure 3 also show the distribution of terrestrial carbon fluxes along latitudes. The poste-
 235 rior and prior fluxes have a similar distribution trend along the latitude, with a significant peak near
 236 60°N, and the peaks of Exp_OCO2 and Exp_OCO3&2 are comparable, which are significantly higher
 237 than the a priori, while Exp_OCO3 has the lowest peak and that is close to the a priori. In addition, it
 238 also could be found that the terrestrial carbon sinks obtained from Exp_OCO3 are also significantly
 239 smaller than those from Exp_OCO2 and Exp_OCO3&2 near 30°S.

240



241

242 **Figure 3.** Spatial distribution of annual mean posterior terrestrial and oceanic carbon fluxes from 2020 to 2022,
 243 the difference between posterior and prior fluxes, and the distribution of terrestrial NEEs at different latitudes.
 244 (a, b, c, Exp_OCO3; d, e, f, Exp_OCO2; g, h, i, Exp_OCO3&2)

245 In order to better understand and compare the differences among different inversion experiments,
 246 we have aggregated the prior and the posterior NEEs into the 11 TransCom-3 land regions (Figure 2),
 247 as shown in Figure 4. It is clearly that almost all terrestrial regions behave as carbon sinks, both prior



248 and posterior fluxes. Among the experiments, only the terrestrial NEE in northern Africa obtained by
249 Exp_OCO3&2 shows a weak carbon source. There is relatively good agreement between all the inver-
250 sion experiments on whether the land carbon flux is a source or sink, but there is significant difference
251 in the NEE values. In all regions except temperate N. America, northern Africa, temperate Asia, and
252 Australia, Exp_OCO3 shows a lower carbon sink than Exp_OCO2. Comparing Exp_OCO3 with
253 Exp_OCO3&2, Exp_OCO3&2 shows stronger carbon sinks in temperate N. America, southern Africa,
254 Australia, and Europe; and weaker sinks in tropical S. America, northern Africa, and boreal Asia; and
255 elsewhere Exp_OCO3&2 shows sinks intermediate to the other two experiments.

256 The regions with more pronounced differences among experiments are temperate S. America and
257 Europe. In Europe, the posterior fluxes of each inversion experiment show a pronounced carbon sink,
258 which is considerably larger than the prior flux, but the results of different experiments vary signifi-
259 cantly, with NEEs ranging from -0.88 to -1.18 PgC yr⁻¹ (Table 2), with Exp_OCO3&2 having the
260 largest sink. In the temperate S. America, Exp_OCO3 exhibits a very weak carbon sink, whereas both
261 Exp_OCO2 and Exp_OCO3&2 show a moderate carbon sink. One potential explanation for this dis-
262 crepancy is that the XCO₂ concentration observed by OCO-3 in the temperate South America is higher
263 than that observed by OCO-2 for the duration of the study period (by ~0.55 ppm). Consequently, in
264 that assimilating the OCO-3 observations yields a weaker carbon sink. Compared with the prior flux,
265 the posterior NEE in the tropical S. America shows a significant discrepancy, the prior flux show a
266 very strong carbon sink of -0.78 PgC yr⁻¹, whereas the subsequent application of constraints from
267 satellite observations resulted in a reduction of the carbon sinks by approximately 2 to 3 times, with
268 values ranging from -0.21 to -0.41 PgC yr⁻¹.

269 Following the imposition of constraints derived from satellite observations, the carbon sinks on the
270 Northern Hemisphere land are all enhanced, with the largest enhancement of 0.59 PgC yr⁻¹ in
271 Exp_OCO3&2, followed by 0.19 and 0.36 PgC yr⁻¹ in Exp_OCO3 and Exp_OCO2, respectively.
272 While in the tropics, the carbon sinks were all weakened, with Exp_OCO3 being weakened most, by
273 0.67 PgC yr⁻¹, and the Exp_OCO2 and Exp_OCO3&2 being weakened by 0.37 and 0.59 PgC yr⁻¹,
274 respectively; on Southern Hemisphere land, in Exp_OCO3, the sinks were weakened by 0.2 PgC yr⁻¹,

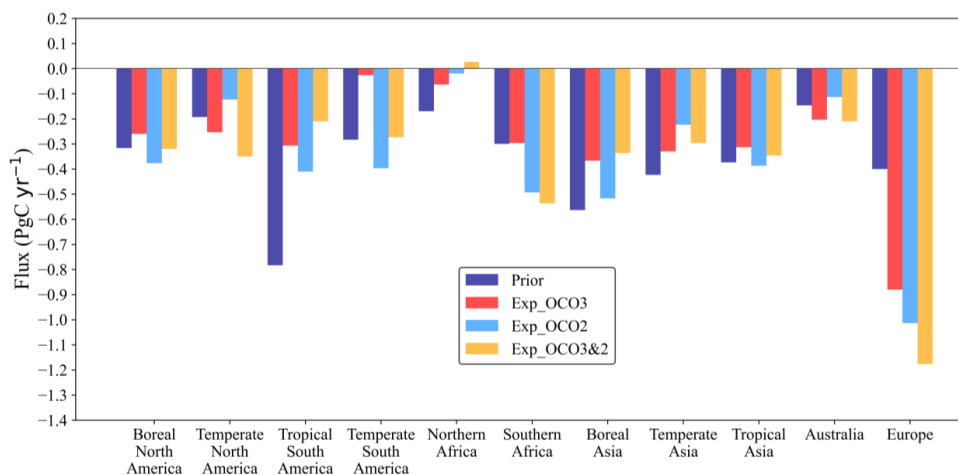


275 whereas in Exp_OCO2 and Exp_OCO3&2, they were enhanced by 0.08 and 0.05 PgC yr⁻¹, respec-
 276 tively.

277 **Table 2.** Annual mean terrestrial fluxes (PgC yr⁻¹) in 2020-2022 for 11 TransCom-3 land regions, as well as for
 278 Northern Hemisphere land, Tropical land and Southern Hemisphere land. Includes the prior flux and the poste-
 279 rior fluxes from three inversion experiments.

Regions	Prior	Exp_OCO3	Exp_OCO2	Exp_OCO3&2
Boreal North America	-0.32	-0.26	-0.38	-0.32
Temperate North America	-0.19	-0.25	-0.12	-0.35
Tropical South America	-0.78	-0.31	-0.41	-0.21
Temperate South America	-0.28	-0.03	-0.40	-0.27
Northern Africa	-0.17	-0.06	-0.02	0.03
Southern Africa	-0.30	-0.30	-0.49	-0.54
Boreal Asia	-0.56	-0.37	-0.52	-0.34
Temperate Asia	-0.42	-0.33	-0.22	-0.30
Tropical Asia	-0.37	-0.31	-0.39	-0.35
Australia	-0.15	-0.20	-0.11	-0.21
Europe	-0.40	-0.88	-1.01	-1.18
Northern Hemisphere lands	-1.89	-2.08	-2.25	-2.48
Tropical lands	-1.65	-0.98	-1.28	-1.06
Southern Hemisphere lands	-0.43	-0.23	-0.51	-0.48

280



281 **Figure 4.** Annual average terrestrial carbon fluxes for the 11 TransCom-3 land regions in 2020-2022.

282 4.3 Seasonal cycle of NEE

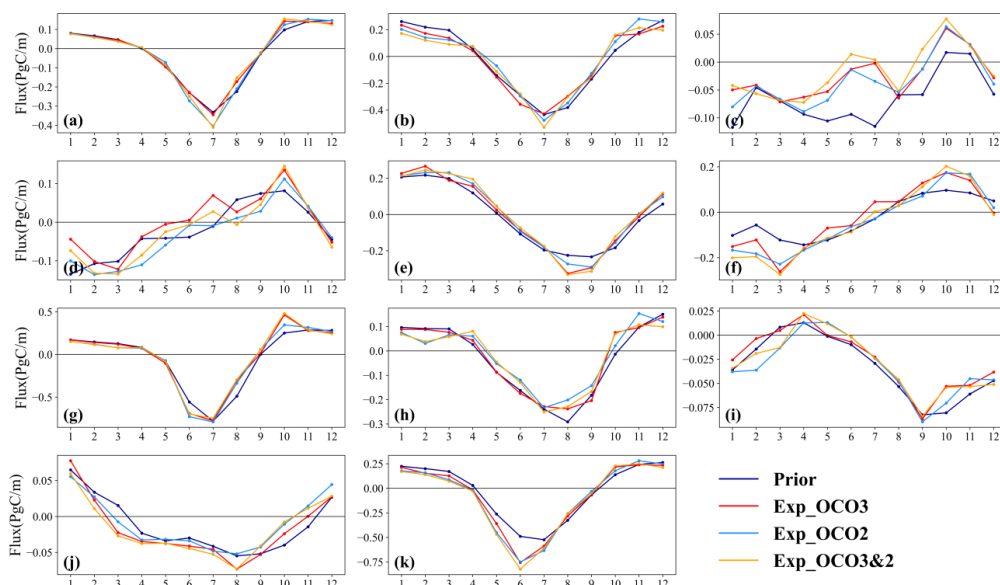
283 Figure 5 illustrates the seasonal cycle of NEE for each TransCom-3 region. The posterior NEEs
 284 of different experiments are in good agreement on the seasonal cycle in most regions. In the Northern
 285 Hemisphere, the seasonal cycles of NEE in boreal N. America, temperate N. America, boreal Asia,
 286 temperate Asia, and Europe show relatively consistent trends. Carbon sinks in these regions generally
 287 occur from May to September and carbon sources from October to April. Significant differences are
 288 evident in the strength of the carbon sinks observed in different regions, with different months in which
 289 the strongest carbon sinks occur. Boreal N. America, temperate N. America, and boreal Asia have the
 290 strongest carbon sinks in July, temperate Asia has the peak in July or August, and Europe has the
 291 strongest sinks in June. In the Southern Hemisphere, the southern Africa and temperate S. America
 292 have more consistent seasonal cycles, with their carbon sources occurring roughly from July to De-
 293 cember and sinks from January to June. The strongest carbon sources all occur in October, and the
 294 strongest sinks occur around March. In Australia, carbon sinks occur mainly from March to October,
 295 with the peak occurring in August. In the tropics, southern Africa shows a seasonal cycle opposite to
 296 that of northern Africa, and carbon sinks occur from January to July with the strongest carbon sinks
 297 occurring near March. Tropical Asia shows a carbon sink in most months, with the strongest sink in
 298 September. The seasonal cycle in tropical S. America is more complex, with the strongest carbon



299 source in October. In general, seasonal amplitudes are small in the tropics and large in the northern
300 regions. The averaged seasonal amplitudes in the boreal Asia, Europe, and temperate N. America are
301 1.17, 0.97, and 0.72 PgC yr⁻¹, respectively, while the seasonal amplitudes in tropical Asia and S. Amer-
302 ica are about 0.10 PgC yr⁻¹.

303 The regions where the difference between the prior and posterior NEEs is particularly pronounced
304 are tropical S. America, southern Africa, Australia, and Europe. In the tropical S. America, the prior
305 NEE is a significant sink from May to July, but after constraints from satellite observations, the carbon
306 sink decreases significantly, even approaching neutral in June and July, and furthermore, in September
307 and October, the sink also decreases significantly compared to the a priori. In southern Africa, the
308 carbon sink is significantly stronger from January to March compared to the a priori, and conversely,
309 the carbon source is significantly stronger in October and November. In Australia, the carbon sink is
310 significantly increased from January to August and decreased in October and November compared to
311 the a priori. In Europe, there is a significant increase in the carbon sinks from May to June compared
312 to the a priori.

313 As described in Section 4.2 that in temperate N. America, northern Africa, temperate Asia, and
314 Australia, Exp_OCO3 shows a stronger sink than Exp_OCO2, which mainly occurs in May and June
315 in temperate N. America, in August and September in northern Africa, from April to September in
316 temperate Asia, and in Australia except for July. In other regions, Exp_OCO3 has weaker sinks than
317 Exp_OCO2. In the high latitudinal regions, on the one hand, the carbon sinks in June and July of the
318 Exp_OCO3 are generally smaller than those of Exp_OCO2, and on the other hand, the carbon source
319 in October is significantly higher than that of Exp_OCO2, while in the tropics, the carbon sink is lower
320 than that of Exp_OCO2 almost all year round. Compared to Exp_OCO3, Exp_OCO3&2 shows
321 stronger carbon sinks in temperate N. America, southern Africa, Australia, and Europe, mainly in sum-
322 mer; and weaker sinks in tropical S. America, northern Africa, and boreal Asia, mainly in autumn.
323 Elsewhere Exp_OCO3&2 shows carbon sinks intermediate to the other two experiments.



324 **Figure 5.** Averaged prior and posterior seasonal cycle of NEE in different TransCom-3 regions during 2020–
 325 2022; (a) boreal N. America, (b) temperate N. America, (c) tropical S. America, (d) temperate S. America,(e)
 326 northern Africa, (f) southern Africa, (g) boreal Asia, (h) temperate Asia, (i) tropical Asia, (j) Australia, (k) Eu-
 327 rope.

328 4.4 Evaluation against independent observations

329 As shown in Figure 6, observations from 66 surface flask sites were used to evaluate the posterior
 330 fluxes. The prior and posterior CO₂ concentrations were simulated by the MOZART-4 model using the
 331 corresponding prior and posterior fluxes, as described in Section 3. The overall assessment results of
 332 the individual inversion experiments on a global scale are shown in Table 3. The results show that the
 333 mean BIAS, MAE, and RMSE between the prior CO₂ concentrations and surface flask observations
 334 are -1.82, 3.27, and 5.01 ppm, respectively. The prior BIAS shows a pronounced negative bias, which
 335 can be attributed to the fact that the prior NEE in 2019 was, on average, approximately 3.5 PgC less
 336 than the posterior NEE. After constraints using the XCO₂ retrievals, the biases of the three experiments
 337 are reduced significantly compared to the a priori, indicating that the surface carbon fluxes have been
 338 improved. A comparison of the three inversion experiments reveals that Exp_OCO3 exhibits the largest



339 BIAS, while Exp_OCO3&2 exhibits the lowest MAE and RMSE.

340

341 **Table 3.** Error statistics between the simulated CO₂ concentrations and surface flask observations (ppm).

342

	BIAS	MAE	RMSE
Prior	-1.82	3.27	5.01
Exp_OCO3	0.32	2.44	4.56
Exp_OCO2	0.02	2.42	4.49
Exp_OCO3&2	0.05	2.34	4.47

343

344

345

346

347

348

349

350

351

352

353

354

355

356

357

358

359

360

361

362

363

364

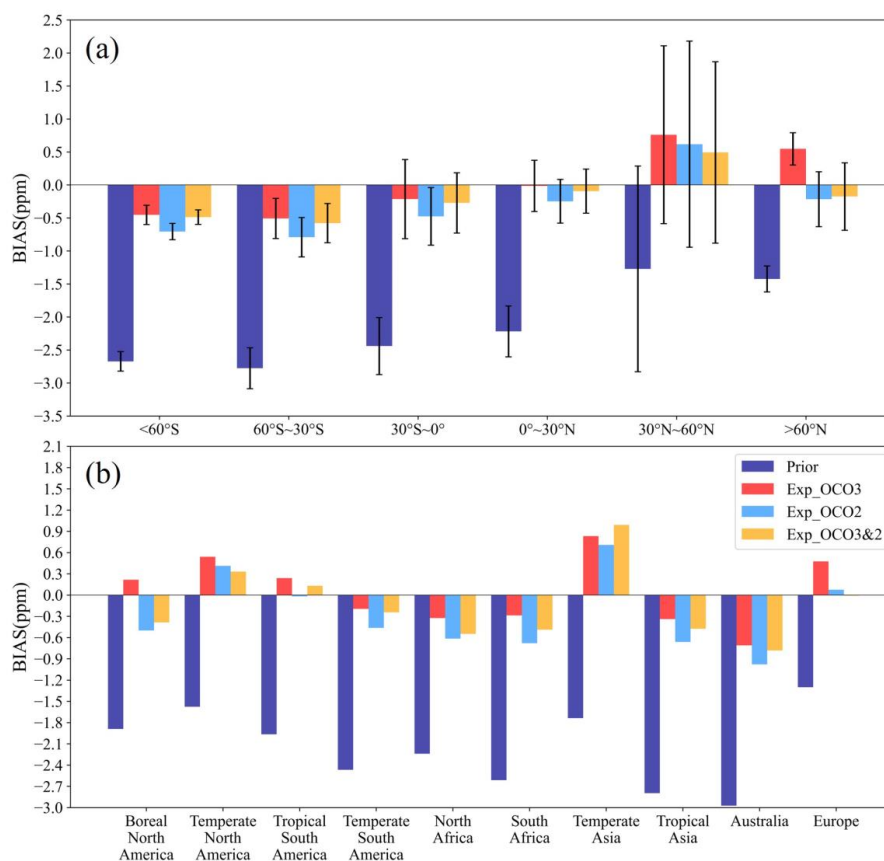
365

366

Figure 6a and 6b illustrate the BIAS of the individual inversion experiments at different latitudinal zones and in different TransCom-3 land regions. In all latitudinal bands and all land regions, the CO₂ concentrations modelled by the a priori fluxes have the largest negative BIAS, which is greater than -1.2 ppm in all cases. Across latitudinal zones, in the Southern Hemisphere, and south of 30°N latitude, the Exp_OCO3 had the smallest BIAS, which is significantly smaller than the Exp_OCO2 and comparable to the results of the Exp_OCO3&2. However, in the mid to high latitudes of the Northern Hemisphere, the BIAS of the Exp_OCO3 is significantly higher than those of the Exp_OCO2 and Exp_OCO3&2. Especially in the region north of 60°N latitude, the Exp_OCO3 exhibits a significant positive BIAS, while the Exp_OCO2 and Exp_OCO3&2 both exhibit small negative BIAS. This suggests that the carbon sinks at mid to high latitudes were underestimated due to the lack of observational data for the OCO-3 north of 52°N latitude. Furthermore, we can find that the BIAS can be further reduced in the mid to high latitudes of the Northern Hemisphere after the addition of assimilated OCO-3 observations compared to the Exp_OCO2. In different TransCom-3 land regions, the BIAS of the three inversion experiments is less than ±0.6 ppm, except in the temperate Asia. In Africa, temperate S. America, tropical Asia, and Australia, the Exp_OCO3 had the smallest BIAS, while the BIAS of Exp_OCO3&2 was between those of Exp_OCO3 and Exp_OCO2. However, in temperate N. America and Europe, the Exp_OCO3 has the largest BIAS, followed by the Exp_OCO2, while the Exp_OCO3&2 has the smallest BIAS. This suggests that since OCO-3 observations are only available



367 between 52 degrees north and south latitudes, assimilating only OCO-3 observations will result in a
 368 significant BIAS in the middle and high latitudes. Conversely, joint assimilation of OCO-2 and OCO-
 369 3 observations can compensate for the limitations of the OCO-3 observations, thereby achieving the
 370 most optimal assimilation outcomes.



371
 372 **Figure 6.** The prior and posterior CO₂ BIAS(a) at different latitudinal zones and (b) in different land
 373 regions.

374

375 **5 Summary and Conclusion**

376 In this study, we constrained terrestrial NEEs for the period 1 August 2019 to 31 December 2022
 377 using the OCO-2 and OCO-3 XCO₂ retrievals and the GCASv2 system, and analyzed the inversion
 378 results from 2020 to 2022. We conducted three inversion experiments for separately and jointly assim-
 379 ilating the OCO-2 and OCO-3 XCO₂ retrievals, to explore the impact of the OCO-3 XCO₂ retrievals



380 on the constraints of global terrestrial NEEs. The prior and posterior CO₂ mixing ratios obtained from
381 forward simulations using the prior and posterior fluxes are analysed in comparison with observations
382 from 66 surface flask sites.

383 Globally, the terrestrial carbon sink from the Exp_OCO3 is smaller than the prior, while the ter-
384 restrial carbon sinks from the other two inversion experiments are slightly larger than the prior, but the
385 difference is small. The global net carbon flux from the Exp_OCO3&2 is very close to the observed
386 atmospheric CO₂ growth rate. Regionally, the posterior NEEs for most terrestrial regions show a car-
387 bon sink, with Europe showing a very strong sink and North Africa close to carbon neutrality. In the
388 Northern Hemisphere, the carbon sinks are enhanced, with the Exp_OCO3&2 being the most enhanced
389 by 0.59 PgC yr⁻¹ and the Exp_OCO3 and Exp_OCO2 by 0.19 and 0.36 PgC yr⁻¹, respectively. In the
390 tropics, the carbon sinks are weakened, with the Exp_OCO3 being the most weakened by 0.67 PgC
391 yr⁻¹, and the Exp_OCO2 and Exp_OCO3&2 sinks being weakened by 0.37 and 0.59 PgC yr⁻¹, respec-
392 tively; in the southern land, the sink inverted in Exp_OCO3 is weakened by 0.2 PgC yr⁻¹, whereas
393 those in the Exp_OCO2 and Exp_OCO3&2 are enhanced, by 0.08 and 0.05 PgC yr⁻¹, respectively.

394 On a global scale, the BIAS between the prior CO₂ concentrations and surface flask observations
395 is -1.82 ppm, with a MAE of 3.27 ppm and a RMSE of 5.01 ppm. The deviations between the posterior
396 CO₂ concentrations and surface flask observations for all three inversions are reduced to different de-
397 grees from the prior, especially for the BIAS, which decreased to 0.32, 0.02, and 0.05 ppm by
398 Exp_OCO3, Exp_OCO2, and Exp_OCO3&2, respectively. This suggests that since OCO-3 only has
399 observations from 52°S to 52°N, assimilating OCO-3 observations alone may lead to an underestima-
400 tion of the terrestrial carbon sink, and the joint assimilation of OCO-2 and OCO-3 XCO₂ retrievals is
401 required for better estimation of the global terrestrial carbon sources and sinks.

402

403 **Code availability.** The code of the GCASv2 system is available to the community and can be accessed
404 upon request from Fei Jiang(jiangf@nju.edu.cn) at Nanjing University.



405 **Data availability.** The OCO-2 and OCO-3 data used in this study is available at [https://www](https://www.earthdata.nasa.gov)
406 [w.earthdata.nasa.gov](https://www.earthdata.nasa.gov). The FOSSIL carbon emissions of GCP-GridFEDv2023.1 is available at
407 <https://doi.org/10.5281/zenodo.8386803>. The FIRE carbon emissions GFED 4.1s is available at
408 https://daac.ornl.gov/VEGETATION/guides/fire_emissions_v4_R1.html. The results of three in
409 version experiments and evaluation are publicly available at [https://doi.org/10.5281/zenodo.112](https://doi.org/10.5281/zenodo.11239535)
410 [39535](https://doi.org/10.5281/zenodo.11239535).

411

412 **Author contributions.** XW and FJ designed the research. XW ran the model, analyzed the results
413 and wrote the paper. HW and ZZ collected the OCO-2 and OCO-3 XCO₂ retrievals. MW, JW, WH,
414 WJ and JC participated in the discussion of the inversion results and provided revisions before the
415 paper was submitted.

416

417 **Competing interests.** The author has declared that none of the authors has any competing interests.

418

419 **Financial support.** This work is supported by the National Key R&D Program of China (Grant No:
420 2023YFB3907404) and the National Natural Science Foundation of China (Grant No. 42377102).

421

422 **Acknowledgments.** The OCO-2 and OCO-3 data are produced by the OCO project at the Jet Propul-
423 sion Laboratory, California Institute of Technology, and obtained from the data archive at the NASA
424 Goddard Earth Science Data and Information Services Center. We acknowledge all atmospheric data
425 providers to obspack_co2_1_GLOBALVIEWplus_v9.1_2023-12-08. We are also grateful to the
426 High-Performance Computing Center (HPCC) of Nanjing University for doing the numerical calcu-
427 lations in this paper on its blade cluster system.

428

429 **References**

430 Basu, S., Guerlet, S., Butz, A., Houweling, S., Hasekamp, O., Aben, I., Krummel, P., Steele, P., Langen-
431 felds, R., Torn, M., Biraud, S., Stephens, B., Andrews, A., and Worthy, D.: Global CO₂ fluxes
432 estimated from GOSAT retrievals of total column CO₂, Atmos. Chem. Phys., 13, 8695–8717,
433 <https://doi.org/10.5194/acp-13-8695-2013>, 2013.



- 434 Botta, A., Ramankutty, N., and Foley, J. A.: LBA-ECO LC-04 IBIS Model Simulations for the Amazon
435 and Tocantins Basins: 1921-1998, <https://doi.org/10.3334/ORNLDAAAC/1139>, 2012.
- 436 Bousquet, P., Peylin, P., Ciais, P., Le Quéré, C., Friedlingstein, P., and Tans, P. P.: Regional Changes in
437 Carbon Dioxide Fluxes of Land and Oceans Since 1980, *Science*, 290, 1342-1346,
438 <https://doi.org/10.1126/science.290.5495.1342>, 2000.
- 439 Byrne, B., Liu, J., Lee, M., Baker, I., Bowman, K. W., Deutscher, N. M., Feist, D. G., Griffith, D. W.
440 T., Iraci, L. T., Kiel, M., Kimball, J. S., Miller, C. E., Morino, I., Parazoo, N. C., Petri, C., Roehl,
441 C. M., Sha, M. K., Strong, K., Velazco, V. A., Wennberg, P. O., and Wunch, D.: Improved con-
442 straints on northern extratropical CO₂ fluxes obtained by combining surface-based and space-
443 based atmospheric CO₂ measurements, *J. Geophys. Res.: Atmos.*, 125, e2019JD032029,
444 <https://doi.org/10.1029/2019JD032029>, 2020.
- 445 Byrne, B., Liu, J., Lee, M., Yin, Y., Bowman, K. W., Miyazaki, K., Norton, A. J., Joiner, J., Pollard, D.
446 F., Griffith, D. W. T., Velazco, V. A., Deutscher, N. M., Jones, N. B., and Paton - Walsh, C.: The
447 carbon cycle of southeast Australia during 2019–2020: Drought, fires, and subsequent recovery,
448 *AGU Advances*, 2, e2021AV000469, <https://doi.org/10.1029/2021AV000469>, 2021.
- 449 Byrne, B., Liu, J., Yi, Y., Chatterjee, A., Basu, S., Cheng, R., Doughty, R., Chevallier, F., Bowman, K.
450 W., Parazoo, N. C., Crisp, D., Li, X., Xiao, J., Sitch, S., Guenet, B., Deng, F., Johnson, M. S.,
451 Philip, S., McGuire, P. C., and Miller, C. E.: Multi-year observations reveal a larger than expected
452 autumn respiration signal across northeast Eurasia, *Biogeosciences*, 19, 4779–4799,
453 <https://doi.org/10.5194/bg-19-4779-2022>, 2022.
- 454 Byrne, B., Baker, D. F., Basu, S., Bertolacci, M., Bowman, K. W., Carroll, D., Chatterjee, A., Cheval-
455 lier, F., Ciais, P., Cressie, N., Crisp, D., Crowell, S., Deng, F., Deng, Z., Deutscher, N. M., Dubey,
456 M. K., Feng, S., García, O. E., Griffith, D. W. T., Herkommer, B., Hu, L., Jacobson, A. R., Janar-
457 danan, R., Jeong, S., Johnson, M. S., Jones, D. B. A., Kivi, R., Liu, J., Liu, Z., Maksyutov, S.,
458 Miller, J. B., Miller, S. M., Morino, I., Notholt, J., Oda, T., O'Dell, C. W., Oh, Y.-S., Ohyama, H.,
459 Patra, P. K., Peiro, H., Petri, C., Philip, S., Pollard, D. F., Poulter, B., Remaud, M., Schuh, A., Sha,
460 M. K., Shiomi, K., Strong, K., Sweeney, C., Té, Y., Tian, H., Velazco, V. A., Vrekoussis, M.,
461 Warneke, T., Worden, J. R., Wunch, D., Yao, Y., Yun, J., Zammit-Mangion, A., and Zeng, N.:
462 National CO₂ budgets (2015–2020) inferred from atmospheric CO₂ observations in support of the
463 global stocktake, *Earth Syst. Sci. Data*, 15, 963–1004, <https://doi.org/10.5194/essd-15-963-2023>,
464 2023.
- 465 Chen, H., He, W., Liu, J., Nguyen, N. T., Chevallier, F., Yang, H., Lv, Y., Huang, C., Rödenbeck, C.,
466 Miller, S., Jiang, F., Liu, J., Johnson, M., Philip, S., Liu, Z., Zeng, N., Basu, S., and Baker, D.:
467 Satellite-detected large CO₂ release in southwestern North America during the 2020–2021
468 drought and associated wildfires, *Environ. Res. Lett.*, 19, <https://doi.org/10.1088/1748-9326/ad3cf7>, 2024.
- 470 Chen, J. M., Ju, W., Ciais, P., Viovy, N., Liu, R., Liu, Y., and Lu, X.: Vegetation structural change since
471 1981 significantly enhanced the terrestrial carbon sink, *Nat. Commun.*, 10,
472 <https://doi.org/10.1038/s41467-019-12257-8>, 2019.



- 473 Crisp, D., Pollock, H. R., Rosenberg, R., Chapsky, L., Lee, R. A. M., Oyafuso, F. A., Frankenberg, C.,
474 O'Dell, C. W., Bruegge, C. J., Doran, G. B., Eldering, A., Fisher, B. M., Fu, D., Gunson, M. R.,
475 Mandrake, L., Osterman, G. B., Schwandner, F. M., Sun, K., Ta-ylor, T. E., Wennberg, P. O., and
476 Wunch, D.: The on-orbit performance of the Orbiting Carbon Observatory-2 (OCO-2) instrument
477 and its radiometrically calibrated products, *Atmos. Meas. Tech.*, 10, 59–81,
478 <https://doi.org/10.5194/amt-10-59-2017>, 2017.
- 479 Crowell, S., Baker, D., Schuh, A., Basu, S., Jacobson, A. R., Chevallier, F., Liu, J., Deng, F., Feng, L.,
480 McKain, K., Chatterjee, A., Miller, J. B., Stephens, B. B., Eldering, A., Crisp, D., Schimel, D.,
481 Nassar, R., O'Dell, C. W., Oda, T., Sweeney, C., Palmer, P. I., and Jones, D. B. A.: The 2015–2016
482 carbon cycle as seen from OCO-2 and the global in situ network, *Atmos. Chem. Phys.*, 19, 9797–
483 9831, <https://doi.org/10.5194/acp-19-9797-2019>, 2019.
- 484 Eldering, A., Boland, S., Solish, B., Crisp, D., Kahn, P., and Gunson, M.: High precision atmospheric
485 CO₂ measurements from space: The design and implementation of OCO-2, 2012 IEEE Aerospace
486 Conference, 3-10 March 2012, 1-10, <https://doi.org/10.1109/AERO.2012.6187176>, 2012.
- 487 Eldering, A., O'Dell, C. W., Wennberg, P. O., Crisp, D., Gunson, M. R., Viatte, C., Avis, C., Braverman,
488 A., Castano, R., Chang, A., Chapsky, L., Cheng, C., Connor, B., Dang, L., Doran, G., Fisher, B.,
489 Frankenberg, C., Fu, D., Granat, R., Hobbs, J., Lee, R. A. M., Mandrake, L., McDuffie, J., Miller,
490 C. E., Myers, V., Natraj, V., O'Brien, D., Osterman, G. B., Oyafuso, F., Payne, V. H., Pollock, H.
491 R., Polonsky, I., Roehl, C. M., Rosenberg, R., Schwandner, F., Smyth, M., Tang, V., Taylor, T. E.,
492 To, C., Wunch, D., and Yoshimizu, J.: The Orbiting Carbon Observatory-2: first 18 months of
493 science data products, *Atmos. Meas. Tech.*, 10, 549–563, [https://doi.org/10.5194/amt-10-549-](https://doi.org/10.5194/amt-10-549-2017)
494 2017, 2017.
- 495 Emmons, L. K., Walters, S., Hess, P. G., Lamarque, J.-F., Pfister, G. G., Fillmore, D., Granier, C.,
496 Guenther, A., Kinnison, D., Laepple, T., Orlando, J., Tie, X., Tyndall, G., Wiedinmyer, C., Baugh-
497 cum, S. L., and Kloster, S.: Description and evaluation of the Model for Ozone and Related chem-
498 ical Tracers, version 4 (MOZART-4), *Geosci. Model Dev.*, 3, 43–67, [https://doi.org/10.5194/gmd-](https://doi.org/10.5194/gmd-3-43-2010)
499 3-43-2010, 2010.
- 500 Enting, I.G., Newsam, G.N. Atmospheric constituent inversion problems: Implications for baseline
501 monitoring. *J Atmos Chem* 11, 69–87, <https://doi.org/10.1007/BF00053668>, 1990.
- 502 Feng, S., Jiang, F., Wu, Z., Wang, H., Ju, W., and Wang, H.: CO Emissions Inferred From Surface CO
503 Observations Over China in December 2013 and 2017, *J. Geophys. Res.: Atmos.*, 125,
504 <https://doi.org/10.1029/2019jd031808>, 2020.
- 505 Friedlingstein, P., O'Sullivan, M., Jones, M. W., Andrew, R. M., Bakker, D. C. E., Hauck, J., Land-
506 schützer, P., Le Quéré, C., Luijkx, I. T., Peters, G. P., Peters, W., Pongratz, J., Schwingshackl, C.,
507 Sitch, S., Canadell, J. G., Ciais, P., Jackson, R. B., Alin, S. R., Anthoni, P., Barbero, L., Bates, N.
508 R., Becker, M., Bellouin, N., Decharme, B., Bopp, L., Brasika, I. B. M., Cadule, P., Chamberlain,
509 M. A., Chandra, N., Chau, T.-T.-T., Chevallier, F., Chini, L. P., Cronin, M., Dou, X., Enyo, K.,
510 Evans, W., Falk, S., Feely, R. A., Feng, L., Ford, D. J., Gasser, T., Ghattas, J., Gkritzalis, T., Grassi,
511 G., Gregor, L., Gruber, N., Gürses, Ö., Harris, I., Hefner, M., Heinke, J., Houghton, R. A., Hurtt,



- 512 G. C., Iida, Y., Ilyina, T., Jacobson, A. R., Jain, A., Jarníková, T., Jersild, A., Jiang, F., Jin, Z., Joos,
513 F., Kato, E., Keeling, R. F., Kennedy, D., Klein Goldewijk, K., Knauer, J., Korsbakken, J. I.,
514 Körtzinger, A., Lan, X., Lefèvre, N., Li, H., Liu, J., Liu, Z., Ma, L., Marland, G., Mayot, N.,
515 McGuire, P. C., McKinley, G. A., Meyer, G., Morgan, E. J., Munro, D. R., Nakaoka, S.-I., Niwa,
516 Y., O'Brien, K. M., Olsen, A., Omar, A. M., Ono, T., Paulsen, M., Pierrot, D., Pockock, K., Poulter,
517 B., Powis, C. M., Rehder, G., Resplandy, L., Robertson, E., Rödenbeck, C., Rosan, T. M.,
518 Schwinger, J., Séférian, R., Smallman, T. L., Smith, S. M., Sospedra-Alfonso, R., Sun, Q., Sutton,
519 A. J., Sweeney, C., Takao, S., Tans, P. P., Tian, H., Tilbrook, B., Tsujino, H., Tubiello, F., van der
520 Werf, G. R., van Ooijen, E., Wanninkhof, R., Watanabe, M., Wimart-Rousseau, C., Yang, D., Yang,
521 X., Yuan, W., Yue, X., Zaehle, S., Zeng, J., and Zheng, B.: Global Carbon Budget 2023, *Earth*
522 *Syst. Sci. Data*, 15, 5301–5369, <https://doi.org/10.5194/essd-15-5301-2023>, 2023.
- 523 Gurney, K. R., Law, R. M., Denning, A. S., Rayner, P. J., Baker, D., Bousquet, P., Bruhwiler, L., Chen,
524 Y.-H., Ciais, P., Fan, S., Fung, I. Y., Gloor, M., Heimann, M., Higurashi, K., John, J., Maki, T.,
525 Maksyutov, S., Masarie, K., Peylin, P., Prather, M., Pak, B. C., Randerson, J., Sarmiento, J.,
526 Taguchi, S., Takahashi, T., and Yuen, C.-W.: Towards robust regional estimates of CO₂ sources
527 and sinks using atmospheric transport models, *Nature*, 415, 626–630,
528 <https://doi.org/10.1038/415626a>, 2002.
- 529 Hall, B. D., Crotwell, A. M., Kitzis, D. R., Mefford, T., Miller, B. R., Schibig, M. F., and Tans, P. P.:
530 Revision of the World Meteorological Organization Global Atmosphere Watch (WMO/GAW)
531 CO₂ calibration scale, *Atmos. Meas. Tech.*, 14, 3015–3032, [https://doi.org/10.5194/amt-14-3015-](https://doi.org/10.5194/amt-14-3015-2021)
532 [2021](https://doi.org/10.5194/amt-14-3015-2021), 2021.
- 533 Hansen, J., Sato, M., Russell, G., and Kharecha, P.: Climate sensitivity, sea level and atmospheric
534 carbon dioxide, *Philos. Trans. R. Soc., A*, 371, <https://doi.org/10.1098/rsta.2012.0294>, 2013.
- 535 He, W., Jiang, F., Wu, M., Ju, W., Scholze, M., Chen, J. M., Byrne, B., Liu, J., Wang, H., Wang, J.,
536 Wang, S., Zhou, Y., Zhang, C., Nguyen, N. T., Shen, Y., and Chen, Z.: China's Terrestrial Carbon
537 Sink Over 2010–2015 Constrained by Satellite Observations of Atmospheric CO₂ and Land Sur-
538 face Variables, *J. Geophys. Res.: Biogeosci.*, 127, e2021JG006644,
539 <https://doi.org/10.1029/2021JG006644>, 2022.
- 540 He, W., Jiang, F., Ju, W., Chevallier, F., Baker, D. F., Wang, J., Wu, M., Johnson, M. S., Philip, S.,
541 Wang, H., Bertolacci, M., Liu, Z., Zeng, N., and Chen, J. M.: Improved Constraints on the Recent
542 Terrestrial Carbon Sink Over China by Assimilating OCO-2 XCO₂ Retrievals, *J. Geophys. Res.:*
543 *Atmos.*, 128, e2022JD037773, <https://doi.org/10.1029/2022JD037773>, 2023a.
- 544 He, W., Jiang, F., Ju, W., Byrne, B., Xiao, J., Nguyen, N. T., Wu, M., Wang, S., Wang, J., Rödenbeck,
545 C., Li, X., Scholze, M., Monteil, G., Wang, H., Zhou, Y., He, Q., and Chen, J. M.: Do State-Of-
546 The-Art Atmospheric CO₂ Inverse Models Capture Drought Impacts on the European Land Car-
547 bon Uptake?, *J. Adv. Model. Earth Syst.*, 15, e2022MS003150,
548 <https://doi.org/10.1029/2022MS003150>, 2023b.
- 549 Iida, Y., Takatani, Y., Kojima, A., and Ishii, M.: Global trends of ocean CO₂ sink and ocean acidifica-
550 tion: an observation-based reconstruction of surface ocean inorganic carbon variables, *J.*



- 551 Oceanogr., 77, 323–358, <https://doi.org/10.1007/s10872-020-00571-5>, 2021.
- 552 Jiang, F., Wang, H., Chen, J. M., Ju, W., Tian, X., Feng, S., Li, G., Chen, Z., Zhang, S., Lu, X., Liu, J.,
553 Wang, H., Wang, J., He, W., and Wu, M.: Regional CO₂ fluxes from 2010 to 2015 inferred from
554 GOSAT XCO₂ retrievals using a new version of the Global Carbon Assimilation System, *Atmos.*
555 *Chem. Phys.*, 21, 1963–1985, <https://doi.org/10.5194/acp-21-1963-2021>, 2021.
- 556 Jiang, F., Ju, W., He, W., Wu, M., Wang, H., Wang, J., Jia, M., Feng, S., Zhang, L., and Chen, J. M.: A
557 10-year global monthly averaged terrestrial net ecosystem exchange dataset inferred from the
558 ACOS GOSAT v9 XCO₂ retrievals (GCAS2021), *Earth Syst. Sci. Data*, 14, 3013–3037,
559 <https://doi.org/10.5194/essd-14-3013-2022>, 2022.
- 560 Jin, J., Lin, H. X., Heemink, A., and Segers, A.: Spatially varying parameter estimation for dust emis-
561 sions using reduced-tangent-linearization 4DVar, *Atmos. Environ.*, 187, 358–373,
562 <https://doi.org/10.1016/j.atmosenv.2018.05.060>, 2018.
- 563 Jones, M. W., Andrew, R. M., Peters, G. P., Janssens-Maenhout, G., De-Gol, A. J., Ciais, P., Patra, P.
564 K., Chevallier, F., and Le Quéré, C.: Gridded fossil CO₂ emissions and related O₂ combustion
565 consistent with national inventories 1959–2018, *Sci. Data*, 8, 2, <https://doi.org/10.1038/s41597-020-00779-6>, 2021.
- 567 Lauvaux, T., Pannekoucke, O., Sarrat, C., Chevallier, F., Ciais, P., Noilhan, J., and Rayner, P. J.: Struc-
568 ture of the transport uncertainty in mesoscale inversions of CO₂ sources and sinks using ensemble
569 model simulations, *Biogeosciences*, 6, 1089–1102, <https://doi.org/10.5194/bg-6-1089-2009>, 2009.
- 570 Liu, J., Bowman, K. W., Schimel, D. S., Parazoo, N. C., Jiang, Z., Lee, M., Bloom, A. A., Wunch, D.,
571 Frankenberg, C., Sun, Y., O'Dell, C. W., Gurney, K. R., Menemenlis, D., Gierach, M., Crisp, D.,
572 and Eldering, A.: Contrasting carbon cycle responses of the tropical continents to the 2015–2016
573 El Niño, *Science*, 358, eaam5690, <https://doi.org/10.1126/science.aam5690>, 2017.
- 574 Miller, C. E., Crisp, D., DeCola, P. L., Olsen, S. C., Randerson, J. T., Michalak, A. M., Alkhaled, A.,
575 Rayner, P., Jacob, D. J., Suntharalingam, P., Jones, D. B. A., Denning, A. S., Nicholls, M. E.,
576 Doney, S. C., Pawson, S., Boesch, H., Connor, B. J., Fung, I. Y., O'Brien, D., Salawitch, R. J.,
577 Sander, S. P., Sen, B., Tans, P., Toon, G. C., Wennberg, P. O., Wofsy, S. C., Yung, Y. L., and Law,
578 R. M.: Precision requirements for space - based data, *J. Geophys. Res.: Atmos.*, 112,
579 <https://doi.org/10.1029/2006jd007659>, 2007.
- 580 Miller, S. M., Michalak, A. M., Yadav, V., and Tadić, J. M.: Characterizing biospheric carbon balance
581 using CO₂ observations from the OCO-2 satellite, *Atmos. Chem. Phys.*, 18, 6785–6799,
582 <https://doi.org/10.5194/acp-18-6785-2018>, 2018.
- 583 Miyazaki, K., Eskes, H. J., Sudo, K., Takigawa, M., van Weele, M., and Boersma, K. F.: Simultaneous
584 assimilation of satellite NO₂, O₃, CO, and HNO₃ data for the analysis of tropospheric chemical
585 composition and emissions, *Atmos. Chem. Phys.*, 12, 9545–9579, <https://doi.org/10.5194/acp-12-9545-2012>, 2012.
- 587 ObsPack: Cooperative Global Atmospheric Data Integration Project: Multi-laboratory compilation of



- 588 atmospheric carbon dioxide data for the period 1957-2022; obspack_co2_1_GLOBALVIEW-
589 plus_v9.1_2023-12-08; NOAA Earth System Research Laboratory, Global Monitoring Labora-
590 tory, <http://doi.org/10.25925/20231201>, 2023.
- 591 Palmer, P. I., Feng, L., Baker, D., Chevallier, F., Bösch, H., and Somkuti, P.: Net carbon emissions
592 from African biosphere dominate pan-tropical atmospheric CO₂ signal, *Nat. Commun.*, 10, 3344,
593 <http://doi.org/10.1038/s41467-019-11097-w>, 2019.
- 594 Peiro, H., Crowell, S., Schuh, A., Baker, D. F., O'Dell, C., Jacobson, A. R., Chevallier, F., Liu, J.,
595 Eldering, A., Crisp, D., Deng, F., Weir, B., Basu, S., Johnson, M. S., Philip, S., and Baker, I.: Four
596 years of global carbon cycle observed from the Orbiting Carbon Observatory 2 (OCO-2) version
597 9 and in situ data and comparison to OCO-2 version 7, *Atmos. Chem. Phys.*, 22, 1097–1130,
598 <https://doi.org/10.5194/acp-22-1097-2022>, 2022.
- 599 Peters, W., Jacobson, A. R., Sweeney, C., Andrews, A. E., Conway, T. J., Masarie, K., Miller, J. B.,
600 Bruhwiler, L. M. P., Pétron, G., Hirsch, A. I., Worthy, D. E. J., van der Werf, G. R., Randerson, J.
601 T., Wennberg, P. O., Krol, M. C., and Tans, P. P.: An atmospheric perspective on North American
602 carbon dioxide exchange: CarbonTracker, *P. Natl. Acad. Sci. USA*, 104, 1892518930,
603 <https://doi.org/10.1073/pnas.0708986104>, 2007.
- 604 Peylin, P., Law, R. M., Gurney, K. R., Chevallier, F., Jacobson, A. R., Maki, T., Niwa, Y., Patra, P. K.,
605 Peters, W., Rayner, P. J., Rödenbeck, C., van der Laan-Luijkx, I. T., and Zhang, X.: Global atmos-
606 pheric carbon budget: results from an ensemble of atmospheric CO₂ inversions, *Biogeosciences*,
607 10, 6699–6720, <https://doi.org/10.5194/bg-10-6699-2013>, 2013.
- 608 Philip, S., Johnson, M. S., Baker, D. F., Basu, S., Tiwari, Y. K., Indira, N. K., Ramonet, M., and Poulter,
609 B.: OCO-2 Satellite-Imposed Constraints on Terrestrial Biospheric CO₂ Fluxes Over South Asia,
610 *J. Geophys. Res.: Atmos.*, 127, e2021JD035035, <https://doi.org/10.1029/2021JD035035>, 2022.
- 611 Piao, S., Wang, X., Wang, K., Li, X., Bastos, A., Canadell, J. G., Ciais, P., Friedlingstein, P., and Sitch,
612 S.: Interannual variation of terrestrial carbon cycle: Issues and perspectives, *Global Change Biol.*,
613 26, 300-318, <https://doi.org/10.1111/gcb.14884>, 2020.
- 614 Randerson, J. T., Van Der Werf, G. R., Giglio, L., Collatz, G. J., and Kasibhatla, P. S.: Global Fire
615 Emissions Database, Version 4.1 (GFEDv4), <https://doi.org/10.3334/ORNLDAAAC/1293>, 2017.
- 616 Takahashi, T., Sutherland, S. C., Wanninkhof, R., Sweeney, C., Feely, R. A., Chipman, D. W., Hales,
617 B., Friederich, G., Chavez, F., Sabine, C., Watson, A., Bakker, D. C. E., Schuster, U., Metzl, N.,
618 Yoshikawa-Inoue, H., Ishii, M., Midorikawa, T., Nojiri, Y., Körtzinger, A., Steinhoff, T., Hoppema,
619 M., Olafsson, J., Arnarson, T. S., Tilbrook, B., Johannessen, T., Olsen, A., Bellerby, R., Wong, C.
620 S., Delille, B., Bates, N. R., and de Baar, H. J. W.: Climatological mean and decadal change in
621 surface ocean pCO₂, and net sea-air CO₂ flux over the global oceans, *Deep Sea Res. Pt. II*, 56,
622 554–577, <https://doi.org/10.1016/j.dsr2.2008.12.009>, 2009.
- 623 Taylor, T. E., O'Dell, C. W., Baker, D., Bruegge, C., Chang, A., Chapsky, L., Chatterjee, A., Cheng, C.,
624 Chevallier, F., Crisp, D., Dang, L., Drouin, B., Eldering, A., Feng, L., Fisher, B., Fu, D., Gunson,
625 M., Haemmerle, V., Keller, G. R., Kiel, M., Kuai, L., Kurosu, T., Lambert, A., Laughner, J., Lee,



- 626 R., Liu, J., Mandrake, L., Marchetti, Y., McGarragh, G., Merrelli, A., Nelson, R. R., Osterman,
627 G., Oyafuso, F., Palmer, P. I., Payne, V. H., Rosenberg, R., Somkuti, P., Spiers, G., To, C., Weir,
628 B., Wennberg, P. O., Yu, S., and Zong, J.: Evaluating the consistency between OCO-2 and OCO-
629 3 XCO₂ estimates derived from the NASA ACOS version 10 retrieval algorithm, *Atmos. Meas.*
630 *Tech.*, 16, 3173–3209, <https://doi.org/10.5194/amt-16-3173-2023>, 2023.
- 631 Thompson, R. L., Patra, P. K., Chevallier, F., Maksyutov, S., Law, R. M., Ziehn, T., van der Laan-
632 Luijkx, I. T., Peters, W., Ganshin, A., Zhuravlev, R., Maki, T., Nakamura, T., Shirai, T., Ishizawa,
633 M., Saeki, T., Machida, T., Poulter, B., Canadell, J. G., and Ciais, P.: Top-down assessment of the
634 Asian carbon budget since the mid1990s, *Nat. Commun.*, 7, 10724,
635 <https://doi.org/10.1038/ncomms10724>, 2016.
- 636 Tilmes, S.: GEOS5 Global Atmosphere Forcing Data, Research Data Archive at the National Center
637 for Atmospheric Research, Computational and Information Systems Laboratory [dataset],
638 <https://doi.org/10.5065/QTSA-G775>, 2016.
- 639 Wang, H., Jiang, F., Wang, J., Ju, W., and Chen, J. M.: Terrestrial ecosystem carbon flux estimated
640 using GOSAT and OCO-2 XCO₂ retrievals, *Atmos. Chem. Phys.*, 19, 12067–12082,
641 <https://doi.org/10.5194/acp-19-12067-2019>, 2019.
- 642 Wang, H., Jiang, F., Liu, Y., Yang, D., Wu, M., He, W., Wang, J., Wang, J., Ju, W., and Chen, J. M.:
643 Global Terrestrial Ecosystem Carbon Flux Inferred from TanSat XCO₂ Retrievals, *J. Remote*
644 *Sens.*, 2022, <https://doi.org/10.34133/2022/9816536>, 2022.
- 645 Whitaker, J. S. and Hamill, T. M.: Ensemble Data Assimilation without Perturbed Observations, *Mon.*
646 *Weather Rev.*, 130, 1913-1924, [https://doi.org/10.1175/1520-0493\(2002\)130<1913:ED-](https://doi.org/10.1175/1520-0493(2002)130<1913:ED-AWPO>2.0.CO;2)
647 [AWPO>2.0.CO;2](https://doi.org/10.1175/1520-0493(2002)130<1913:ED-AWPO>2.0.CO;2), 2002.
- 648 Zhang, S., Zheng, X., Chen, J. M., Chen, Z., Dan, B., Yi, X., Wang, L., and Wu, G.: A gl
649 obal carbon assimilation system using a modified ensemble Kalman filter, *Geosci. Model*
650 *Dev.*, 8, 805-816, <https://doi.org/10.5194/gmd-8-805-2015>, 2015.